energies

MDPI

Article

A Novel Mesoporous Activated Carbon Derived from *Calliandra calothyrsus* via Physical Activation: Saturation and Superheated

Nur Adi Saputra [1,2], Saptadi Darmawan [2], Lisna Efiyanti [2], Djeni Hendra [2], Santiyo Wibowo [2], Adi Santoso [2], Djarwanto [2], Gusmailina [2], Sri Komarayati [2], Dian Anggraini Indrawan [2], Yuniawati [2], Deded Sarip Nawawi [1], Akhiruddin Maddu [3], Gustan Pari [2] and Wasrin Syafii [1,*]

[1] Department of Forest Product, IPB University, Kampus Dramaga, Bogor 16680, Indonesia
[2] National Research and Innovation Agency, Jl. Raya Bogor KM 46, Bogor 16911, Indonesia
[3] Department of Physics, IPB University, Kampus Dramaga, Bogor 16680, Indonesia
* Correspondence: wasrinsy@apps.ipb.ac.id or nadisaputra@gmail.com

Abstract: In this work, both pyrochar and activated carbon were prepared by physical activation (i.e., saturation and superheated) by involving a thermal agent as a comparison. The effects of three agents on the pore development of activated carbon from a new material, *Calliandra calothyrsus*, were observed in detail. The BET surface area and the iodine index of the prepared activated carbon were used as pyrochar selection. Proximate, ultimate, XRD, FTIR, TGA, and SEM were used to characterize the physical and chemical properties of the product. Pyrochar pores were found to develop significantly at 350 °C, indicated by an increase in the BET surface area and iodine index. Pyrochar from a temperature of 350 °C was then selected as a precursor of activated carbon. S–SS and SS–S activated carbon samples were declared to have the highest iodine index (870 mg/g) and the highest BET surface area (642 m^2/g), respectively. The pore distribution data showed that the superheated agent widened the pore and provided an active site for iodine adsorption, while the saturation agent resulted in a narrower pore for an increase in the BET surface area. S–SS has a lower C fraction and higher O fraction than SS–S. The SS–S samples have both Vol and Vol_{mic} for an increased BET surface area. The number of aromatic layers and –OH functional groups of the S–SS sample is more convenient for iodine enhancement than for increasing the BET surface area. Less water droplets and greater energy from superheated resulting pores widen, increasing the aromatic layer and providing additional functional groups.

Keywords: activated carbon; physical activation; steam; superheated; red calliandra

check for updates

Citation: Saputra, N.A.; Darmawan, S.; Efiyanti, L.; Hendra, D.; Wibowo, S.; Santoso, A.; Djarwanto; Gusmailina; Komarayati, S.; Indrawan, D.A.; et al. A Novel Mesoporous Activated Carbon Derived from *Calliandra calothyrsus* via Physical Activation: Saturation and Superheated. *Energies* **2022**, *15*, 6675. https://doi.org/10.3390/en15186675

Academic Editors: Suraini Abd-Aziz, Juferi Idris and Mohamad Faizal Ibrahim

Received: 13 August 2022
Accepted: 8 September 2022
Published: 13 September 2022

Publisher's Note: MDPI stays neutral with regard to jurisdictional claims in published maps and institutional affiliations.

Copyright: © 2022 by the authors. Licensee MDPI, Basel, Switzerland. This article is an open access article distributed under the terms and conditions of the Creative Commons Attribution (CC BY) license (https://creativecommons.org/licenses/by/4.0/).

1. Introduction

Porous carbon, with inherently good surface properties, is widely used in various special applications such as rhodamine blue [1], nitrates [2], gases [3], methylene blue [4], toluene [5,6], metals [7,8], iodine [9], and COD removal [10]. Considering the simplicity and stock in nature, biomass is a potential candidate for producing mesoporous activated carbon. Exploration of new species of biomass is carried out continually to locate candidates that have adequate basic characteristics such as activated carbon material. The requirements for physical and chemical properties may be applied more precisely as a basis for selection. The characteristics of the raw materials greatly affect the prepared pyrochar or activated carbon [11].

Activated carbon can be produced from various types of biomass, both in the form of waste and raw materials. The determination of biomass as a precursor of activated carbon is due to its accessibility, low cost and good adsorption efficiency [12]. The adsorption property is strongly influenced by the type of raw material and the specified pyrolysis parameters. Since the nature of the raw material is given, the pyrolysis parameters are

often the focus of the study. In general, time and temperature parameters regulate both carbonization and the activation of activated carbon. At the activation level, the type of activator and sample preparation are defined to affect the quality of the product. Activating agents for the production of activated carbon are divided into two physical and chemical groups. Chemical agents such us H_3PO4 have been involved in activated carbon production [13]. The prepared activated carbon generated a high surface area of 2132.1 m^2/g, and a large volume of 3.426 cm^3/g. The activation of carrageenan by KOH results in a superior surface area. Alkali metal impregnation generates a surface area of more than 2500 m^2/g at an activation temperature of 900 °C [14]. Oil palm empty fruit biomass has been tested as an activated carbon material for supercapacitor applications. Nitrogen impregnation from urea produces a surface area of ~640 m^2/g and a capacitance of 176 F/g, from activated carbon produced at 800 °C [15]. Activation of agricultural biomass, namely sugar cane bagasse and sunflower seed hulls by phosphoric acid and zinc chloride at low temperatures produces a surface area above 2200 m^2/g [9]. Some researchers conduct studies through physical activation pathways that are more environmentally friendly. The activation of bamboo by steam at a temperature of 850 °C produces a surface area above 2000 m^2/g [16]. Barley straw was determined as activated carbon material by a carbon dioxide agent at 800 °C. The prepared activated carbon has a surface area of 789 m^2/g [17]. At higher temperatures, steam–activated pine nut shell produces a surface area of 1057 m^2/g [18]. A mixture of materials may be preferable due to the abundant various biomass in nature. Activated carbon from a mixed biomass at 900 °C produces a surface area of 1025 m^2/g [19]. The utilization of agricultural biomass–based waste includes a circular economic effort. Rice husk activated at 800 °C by steam resulted in a high surface area of 1365 m^2/g [20]. Materials from biomass processing such as phenolic fibre or spherical phenol resin generate high surface areas of 2938 and above 2600 m^2/g, respectively [21,22]. In general, the quality of activated carbon resulting from physical activation has a lower surface area than that resulting from the chemical [23]. However, the cost efficiency and simplicity of the process may be preferred for mass production.

One of the biomasses for producing activated carbon that has never been used is red calliandra (*Calliandra calothyrsus*), which has been known as the material for making charcoal. Red calliandra charcoal may produce 7200 kcal/kg of heat [24], so it is suitable for use as an energy source. This species has adapted well in various habitats and has a diversified ecological benefit [25]. The cellulose, hemicellulose, and lignin content of red calliandra were 44.54, 19.35, and 27.31%, respectively [26]. This adequate lignin content is advantageous when red calliandra is prepared to produce pellets [27] to increase the calorific value [28]. Despite the effect on energy characteristics, the removal of chemical content leaves empty capillaries or pores. The lignin component may have been prescribed as the dominant contributor to the determination of the pore characteristics of charcoal and activated carbon [29]. As summarized above, the production of activated carbon by physical agents may be more affordable for mass production. Physical–steam activation has been conducted by many scholars previously. However, it is important to note that the steam used is saturated steam which still has water droplets and has the potential to reduce energy in the operational reactor. At this point, process engineering to convert the saturated steam to more heating energy, later known as superheated steam, may require further exploration.

In addition, an alternative known as superheated steam is further developed–based saturated. The superheated condition indicates steam reheating leading to passage through the saturation curve to reduce small water droplets. The technology has been used to extract, modify, improve, and produce essential oils [30], biomass refineries [31], dry sawdust [32], polyethylene density [33], and rice quality [34]. According to a previous study, superheated steam was denoted effectively in accelerating the main polymer decomposition [35]. The pathway of superheated–released derivatives was also reported, with the pyrolysis behaviour being subsequently complemented [36].

Nonetheless, pore development by superheating has not been defined to be further discussed. Understanding the inherent pore characteristics led to distinct goals. Therefore, the present study aims to investigate the activated carbon character produced from the new material of red calliandra. For the effectiveness of pore development, activated carbon from red caliandra was synthesized, and the effect of three types of activating agents (thermal, steam and superheated) were studied in detail in the carbonization and activation stages. In addition, the structure of the prepared activated carbon was characterized to provide a relationship between its structure and pore development through the iodine adsorption capacity. A series of adsorption experiments have been carried out and the resulting adsorption isotherms have been described using the nitrogen adsorption model (BET). The iodine adsorption also presented to observe adsorption behaviour. This work provides a modification of the activated carbon production process for improved adsorption performance in a simple industrial operation.

2. Experimental

2.1. Materials and Preparation

C. calothyrsus was selected as the raw material for activated carbon production, related simplicity cultivated in various areas and the amount of abundance in nature. The proximate, ultimate, and wood chemistry analyses are shown in Table 1. Proximate analysis used the Indonesian National Standard (INS) measurement method 06–3730–1995, with the ultimate test subsequently utilizing the elemental instruments, hemicellulose (Cross and Bevan technique), and lignin Klason procedure [37,38]. In the present study, material solubility characteristics were calculated using the procedure of The Technical Association of Pulp and Paper Industry (TAPPI). The solubility of hot and cold water, NaOH, as well as alcohol-benzene were 5.64, 4.29, 16.27, and 4.89%, respectively.

Table 1. The raw materials characterization: proximate, ultimate, and chemical.

Proximate			Ultimate				Wood Chemical		
Volatile	**Ash**	**FC**	**C**	**H**	**N**	**O**	**Hemicellulose**	**Cellulose**	**Lignin**
77	1.2	18	45.23	6.32	0.63	47.82	29.9	58.36	28.8

2.2. Experimental Procedure

Red calliandra has been chosen as the material for this study. Based on the new material, a temperature sequence was applied to determine pore formation in carbonization. The temperature of 250–500 °C was applied to dry pyrolysis at a 50 °C interval for 1 h resident time. The temperature above 200 °C was based on the previously reported effective decomposition of most susceptible polymers [35]. Biochar activation was carried out at a temperature of 800 °C for 1 h final resident time. Furthermore, carbonization and activation used variations of thermal treatment, as well as saturated and superheated steam. The achievement of the superheated steam condition was maintained by heating the steam to 450 °C.

The general procedure is described below. Red calliandra was obtained from the research area of the Research and Development Agency, Ministry of Forestry, in dry season 2021. The main stem diverged into four parts in longitudinal orthotopic direction, about 30 cm long, with branches and twigs excluded from samples. Subsequently, material was air–dried for one week through natural dehydration, then crushed to a 40–mesh size. Fine powder was dried at 105 °C for 18 h to avoid moisture and condensation in the experiment. The powder was then characterized by proximate, elemental (C, H, O, N), and wood chemistry, before being fed to an electric stainless steel reactor. Approximately 900 g of powder was placed into the reactor. The pyrolysis apparatus were engineered at Forest Product (FORPRO) R&D Centre for producing activated carbon. The samples were heated to the target temperature, accompanied by saturated/superheated steam flow at a pressure of 2 bar for 1 h. After final residence time, samples were left in the reactor for 18 h and placed in an oven to avoid direct contact with the environment.

To facilitate identification, samples are labelled as described below. Both carbonization and activation involve the same treatment: thermal (T), saturation (S) and superheated (SS). A series of temperature treatments are applied in the carbonization from 250–500 C with an interval of 50 °C. Thus, the pyrochar produced from a temperature of 450 °C through SS is noted as SS450. Pyrochar originating from 350 °C are then activated at 800 °C for 1 h by applying the same treatment (i.e., T, S, and SS). Therefore, the S-assisted pyrochar which is then activated by SS is recognized as S–SS.

2.3. Product Characterization

The proximate analysis and iodine adsorption followed the Indonesian National Standard (INS) 06–3730–1995, concerning Technical Activated Carbon. Briefly, the temperatures applied for volatile calculation, moisture, and ash content were 950, 115, and 900 °C, respectively. Iodine adsorption was carried out by heating 0.5 g of biochar at 115 °C for 1 h. This sample was then pipetted to 50 mL of 0.1 N iodine solution and stirred for 15 min. The solution was subsequently placed into a centrifugal tube and rotated for 5 min until the filtrate was separated from the precipitate. A total of 10 mL filtrate was then pipetted and added to 30 mL distilled water, through the titration method with 0.1 N $Na_2S_2O_3$ solution.

The structural properties were analysed using a Shimadzu 7000 with a Cu source. The morphology was observed by a Carl Zeiss SEM EVO 50 with 1000× magnification, as an energy of 20 kV. Moreover, surface area, volume, and distribution were calculated by measurement of the N_2 adsorption/desorption, with the sample being removed from resident gas at 300 °C for 1.5 h under vacuum conditions. Further analysis was then carried out using pure N_2 as the adsorbate gas. Functional group analysis was conducted through the mixing of a 4 mg sample with 200 mg KBr. Pellets were subsequently produced with a diameter, thickness, and compression of 1.3 cm, 0.5 cm, and six tons, respectively. Subsequently, the absorption measurement operated the Bruker Tensor FTIR infrared spectrum, with data obtained as transmission at 400–4000 cm^{-1}.

3. Results and Discussion

3.1. Chemical Properties of Raw Material, Char and Activated Carbon

Pyrolysis applied a regime of 250–500 °C with 50 °C intervals. The 1 h resident time was restricted to producing pyrochar with sufficient porosity [39]. In this study, resident variation was not applied due to prolonged contributing less to pore development [40].

The raw materials have volatile, ash and fixed carbon of 77, 1.2 and 18%, respectively. If the proximate character compared to previous reports [41], red calliandra has the potential as an activated carbon material. Thermochemical conversion alters this composition to produce porous material. Activation is initiated by pyrolysis of the feedstock to achieve carbon–rich materials, subsequently pores development to enhanced adsorption properties. Figure S1 shows the proximate properties of pyrochar and activated carbon. The pyrochar yield decreased with temperature interval based on the severe reaction between material and thermal/steam (saturation and superheated), in other side, number of carbon atoms was observed to be increased. Volatile degradation also indicated the mass decline, as shown in Figure S1c. The massive volatiles release and an increase in gas volume were also observed for a reduction in mass [18]. Char yield dramatically decreased above 250 °C, leading to a reduction in mass based on basic polymer decomposition [35]. The highest to lowest of pyrochar yields were thermal, saturation, and superheated, respectively.

The content of C–fraction was closely and contiguously affected by temperature. However, a T300 anomaly indicated that fixed carbon (FC) declined compared to saturation and superheated steam. The thermal method was predicted to be incapable against the H_2O and gases chain reactions, resulting in smaller water molecules being trapped in the carbon structure. A similar phenomenon was also demonstrated by pyrolysis at 400 °C (S400), which further led to FC degradation. Ash content corresponded to raised temperature [42], while moisture was affected by the pyrolysis agent. Acid leaching may aid in reducing the ash content of the raw material, particularly the dissolved fraction and provided extra

oxygen groups [43]. A gradual volatile drop was strong evidence of polymer decomposition complemented by an increase in FC in higher pyrolytic temperatures. These results were found to be in line with previous studies [44,45], as the purification of fraction C and volatile reductions were employed as indicators of carbonization degree accelerated by temperature. Oxidation rate and residence time were claimed to impact the char–produced quality [46]. Pyrolytic temperature ~390 °C was dominated by cellulose degradation, leading to a decrease in mass [47]. Hemicellulose and cellulose decomposed below 500 °C, while lignin decomposed at higher temperatures and was followed by a slow decrease in mass [18]. Volatile and FC parameters had a linear relationship with temperature in dry pyrolysis. Therefore, the intermediate temperature pyrolytic char of 350 °C was then selected for activation, taking into account an adequate surface area.

Pyrochar was activated with different activating agents at 800 °C for 1 h, the thermal comparator, as well as saturated and superheated steam, was devoted. The proximate characteristics of activated carbon are shown in Figure S1. The S–SS sample has the lowest yield. However, the sample had extreme ash content assigned by a reduction in mass due to the burn–off effect. This finding confirms superheated presume, which had more energy compared to saturation. As a C–purification pathway, the activation terminology was adequately demonstrated via thermal conversion resulting in high FC. The data was confirming a previous study, based on volatiles removal and pyrolytic gas from the char precursor [48]. Furthermore, the presence of volatiles remaining in pores inhibited growth and reduced the BET surface area [49]. The present study views mass reduction above 70% as evidence of intense volatile evaporation.

3.2. Elementary Contecture

The elemental are reported in Figure 1, where aromaticity and polarity may be determined. All samples had similar aromaticity denoted by closed H/C ratios, while S–SS have the greatest polarity. Due to the highest O/C, S–SS subsequently demonstrated the highest iodine adsorption. The O_2 presence accelerated pyrolysis, as well as increased aromatic rings and porosity [46]. Furthermore, the superheated activation produced satisfactory oxygen functionality based on the increased O–elements.

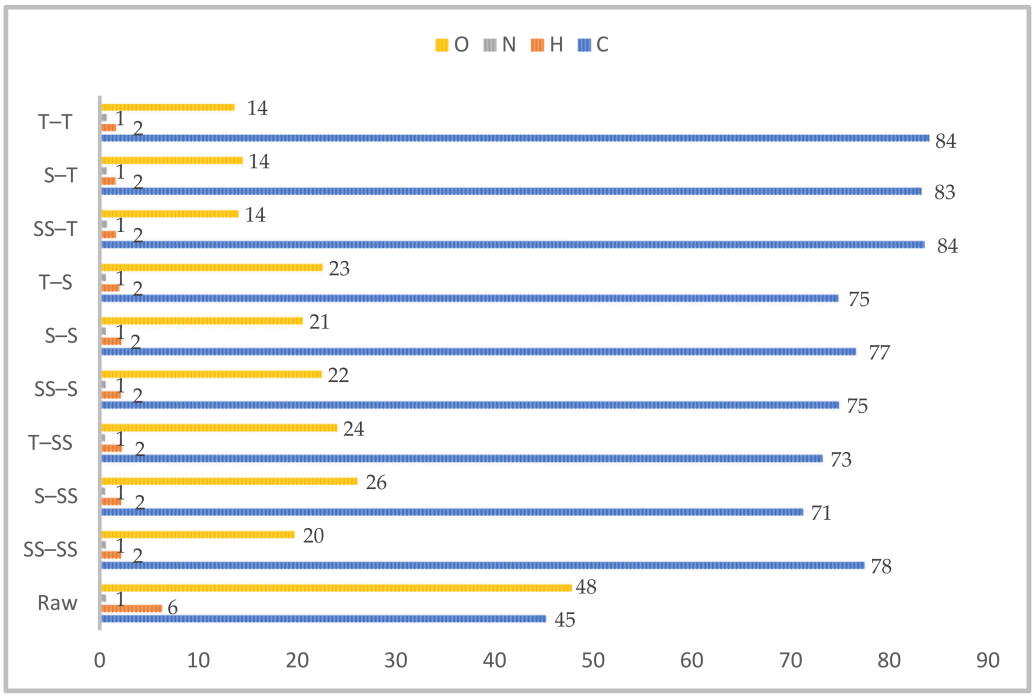
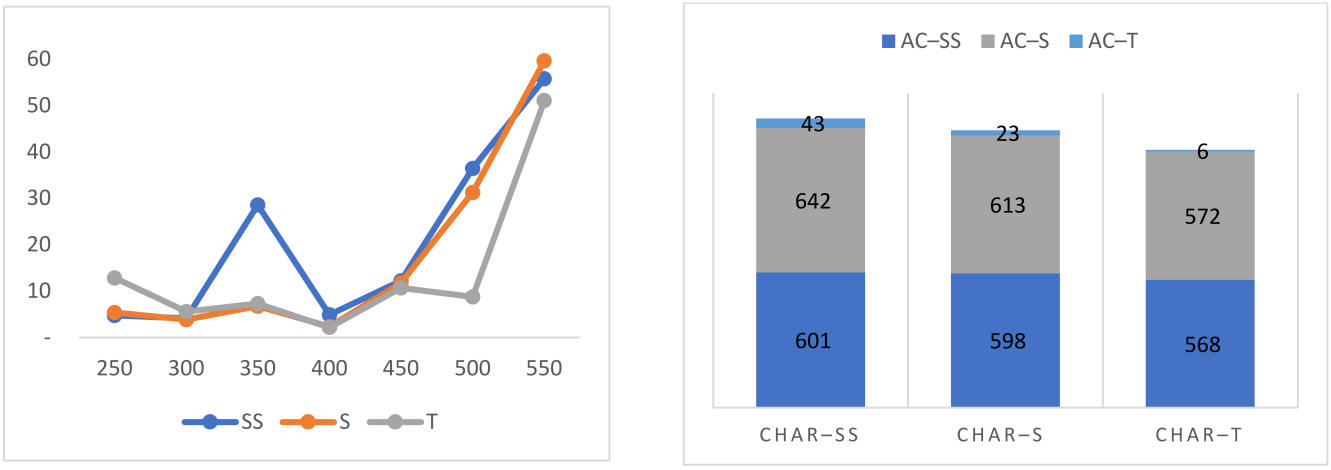


Figure 1. Elemental composition of C, H, N, O in raw and activated carbon.

Activated carbon produced by saturation and superheating has a similar composition of C atoms and is lower compared to thermal treatment. Both saturated and superheated steam provide large amounts of O atoms, thereby lowering the relative portion of C atoms. The pyrolysis temperature converts H and O content into gas and liquid form [50]. The C–derived fraction led to an increase in aromatic layer height (Lc) and an increase in the number of layers (N), which was confirmed by XRD structure analysis.

3.3. Surface Texture Property

The textures properties observed by the BET is shown in Figure 2. An enhancement was observed in all pyrochar parameters to activated carbon, barring for narrowed pores. The quality of the carbonization and activation products were strongly influenced by saturation, thermal, and superheated assistance. Resident variation omitted in this study corresponds to some previous research [17,49]. The pores' creation from carbonization to final activation was characterized by the volatile removal into pyrolytic gases and liquids, while solid residues were allowed to remain. The initial superheated–assisted pore creation reached a significant increase at a temperature of 350 °C confirmed by an increase in BET surface area, then decreased to extend a second increment at 500 °C. Meanwhile, saturation and thermal pyrolysis prepare for the pore creation at higher temperatures. The effectiveness of superheating is recognized as a catalyst for the pore development in pyrolysis. The interfered condition of pore creation may be due to porosity–resisting ash [51,52]. The finding supports the argument that ash decreases slightly after melting (see Figure S1d), and then the surface area further increases gradually. For adsorbent applications, this product may be selected earlier. The medium temperature pyrolysis of 350 °C was then selected as the activated carbon precursor due to adequate surface area.



(**a**) (**b**)

Figure 2. BET surface area in m^2/g. (**a**) pyrochar, (**b**) activated carbon.

The evolution of BET surface area was discovered in this study, varying from approximately 2.91–36.47 and 6–642 m^2/g on char and activated carbon, respectively. In pyrolytic, some selected samples represent models for surface area alterations. SS250, SS350, and SS450 had BET surface areas of 4.75, 28.57, and 12.23 m^2/g, which were subsequently increased to 36.47 m^2/g by SS500. In general, porosity follows an increase in temperature treatment [49,53], whereas this study indicates a condensation in pores development which intention be reconstructed in the next sequence. A similar derivative was shown in previous studies [54], meaning a declined surface area. In this study, pore collapse and fusion were denoted by the presence of mesopore, which was caused by the boundaries to release lignocellulose from the origin material. Hemicellulose and cellulose removal happened at low to medium temperature, while recalcitrant lignin occurred at a higher temperature. Based on this assumption, the initial porosity was then segmented by cellulose removal,

accompanied by lignin released at a subsequent stage. The release of light volatiles indicates the wood chemical decomposition process below 500 °C [17]. Under distinct conditions, ash increment by volatile reduction indicates that pore development became stagnant and collapsed, as observed in the S400 or T300. The increase in ash content induces pore collapse and a decline in surface area [20,53]. The theory of melting ash and tar [18] may be discussed further. In addition, as an explanation for SS350, the initial exposure of the lignin aromatic ring to the subsequent reaction may provide a sufficient argument.

The creation and development of the surface area were interestingly observed, where three pyrolysis agents had distinct effects on the activated carbon properties. In pyrolysis of 350 °C, superheating increases BET surface area significantly compared to steam and thermal. In fact, superheating provides the highest BET surface area in each temperature regime. In the early stages of pyrolysis, all three agents provided a width pore diameter and low volume, followed by porous narrowing and deepening to produce an increase in the BET area. This attribute indicated that mesopores played an important role in carbonization, which was further enhanced in activation through Vol_{mic} variations to increase the BET surface area. The pore complexity is the unique property of porous activated carbon.

Nitrogen adsorption analysis was undertaken to estimate changes in surface area and pore development formed by the applied treatment. Figure 3 shows the activated carbon porosity analysed with N_2 adsorption–desorption. The isotherm slope and hysterical loops were observed at low pressure and the P/P_0 region above 0.4, respectively. This isotherm curve was found to broaden at higher pressures (P/P_0 > 0.4) until P/P_0 = 0.9, based on the capillary condensation of the mesoporosity. According to the IUPAC categories the classification of isotherms was type IV for mesopores adsorbent. The loops displayed belonging to H4 due to having a narrow neck and the better apparent uptake at low P/P_0 being correlated with the stuffing of micropores.

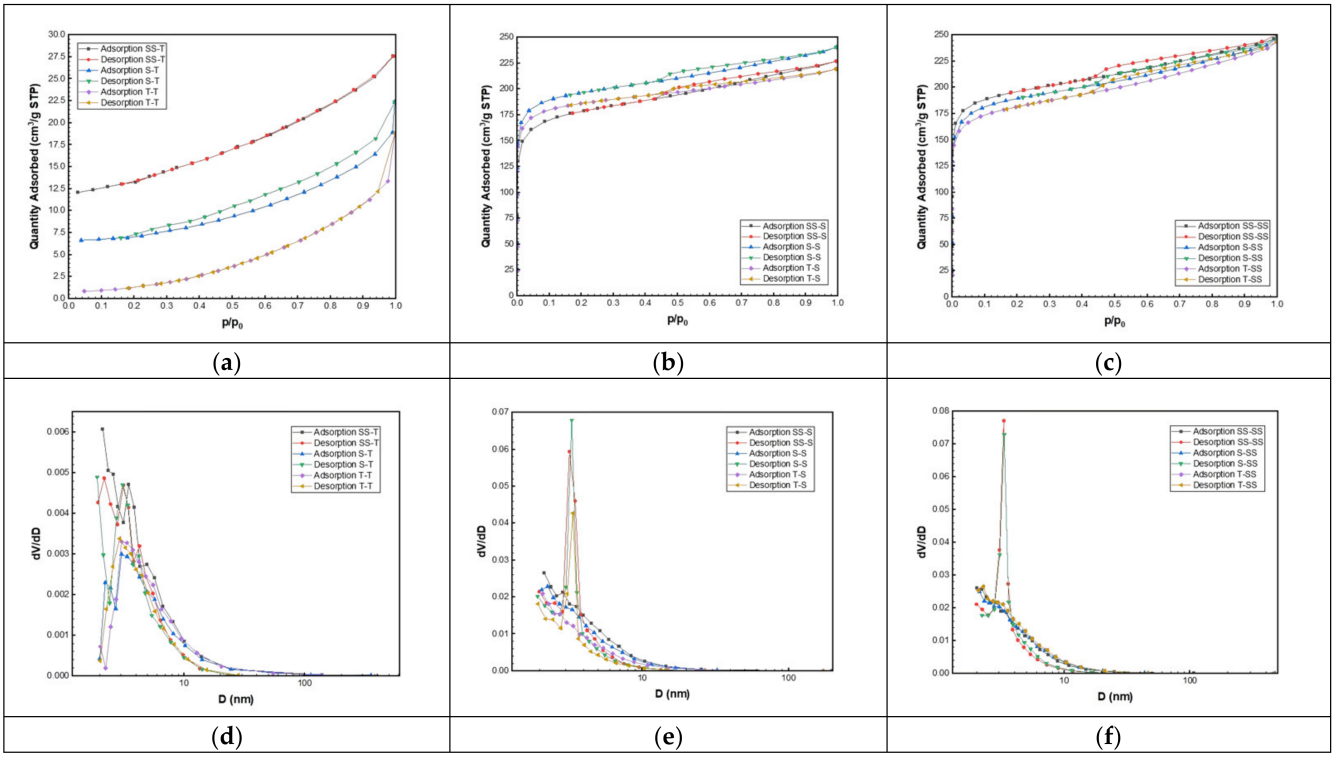


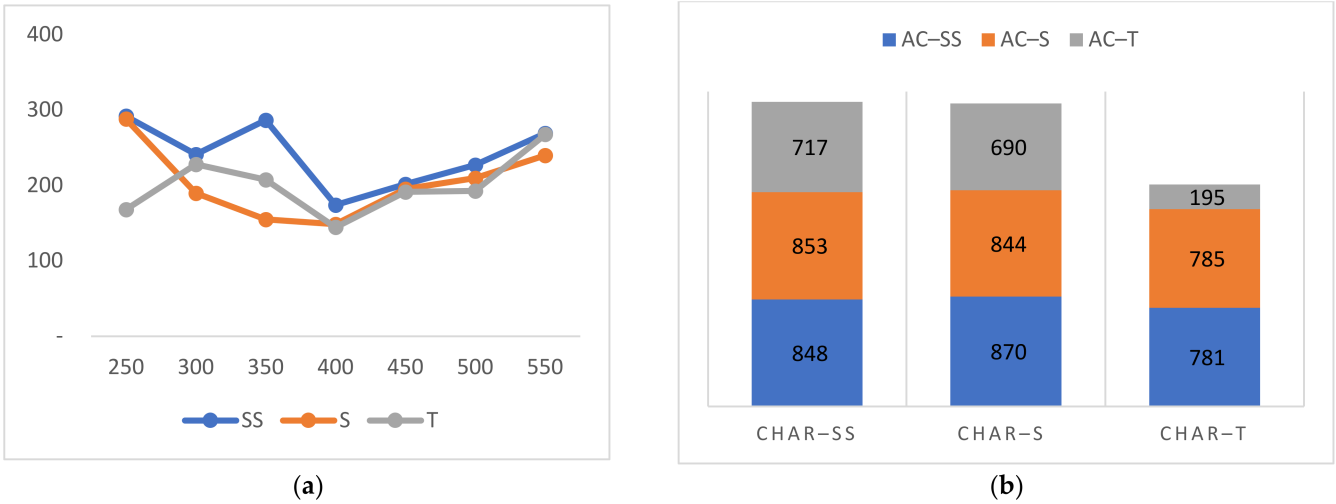
Figure 3. Nitrogen adsorption–desorption isotherm and pore size distribution of prepared activated carbon. (**a**,**d**) thermal activation; (**b**,**e**) saturated steam activation; (**c**,**f**) superheated steam activation.

The isotherm of activated carbon treated by the steam (saturated and superheated) increases sharply at pressures below 0.1 P/P_0. The phenomenon indicates the creation of

micro and mesopores due to the release of volatiles from the pyrochar material. The benefits of superheating to remove gases from the surface of the material in the carbonization stage are very clear. The dominance of small mesopores (2–10 nm) was expressed by the BJH pore distribution report (Table S1). In the thermal group, SS–T produced the highest BET surface area and iodine adsorption of 43 m^2/g and 716 mg/g, respectively. The T–S product produced higher mesopores than other samples in the saturated steam activation group. However, the highest BET area and iodine were expressed by SS-S, namely 642 m^2/g and 853 mg/g. The pore combination that is more complex than SS–S causes an increase in the BET area. The presence of micro–meso pores accelerates the increase in BET area [17]. On the other hand, Vol and Vol_{mic} of SS–S are the highest compared to all samples. Therefore, the finding of the present study is that the BET surface area is strongly influenced by both the diameter and pore volume parameters. A similar phenomenon was found in the superheated activation group. The good diameter and pore volume caused an increase in the BET area of the SS–SS product. The highest iodine adsorption of all samples belonging to S–SS is 870 mg/g. The combination of saturated in the pyrolysis step and the superheated agent in the activation contributed the highest elemental O fraction for the iodine ion adsorption reactivity.

3.4. Iodine Adsorption Performance

Iodine adsorption performance is represented in Figure 4. The findings showed that the iodine index ranged between 144–291 and 195–870 mg/g on pyrochar and activated carbon, respectively, indicating the adsorption capacity of new formed pores [55]. Steam–assisted pyrochar (saturated and superheated) produced the highest iodine adsorption at a low temperature of 250 °C, while the thermal was obtained at 300 °C. This meant that the severe interaction between steam and material determined the attainment of the iodine adsorption. The combination of saturation–superheated (S–SS) delivered the highest iodine adsorption capacity. While S char surface has abundant hydroxyl groups (–OH) thereafter increasing the adsorption ability [56]. Volatile removal aims to increase porosity [57]. This study defines reasonably the shift in the surface texture, including the creation, widening, and cavity of pores through 3 different activating agents. The pores structure contributed to the adsorption properties of iodine ions at 0.532 nm [57].



(**a**) (**b**)

Figure 4. Iodine adsorption performance mg/g. (**a**) pyrochar, (**b**) activated carbon.

The results revealed higher iodine adsorption compared to the surface area since it provided more sites for low electropositive halogens. This is in contrast to the surface area, which is sensitive to shifts in distribution, pore size and volume. For better understanding, several samples were defined as illustrations. It is worthy of note that the pyrochar sample originated from a temperature of 350 °C. Superheated–based pyrochar produced

the highest surface area for both saturation and superheated activation, even SS–S had the highest BET (642 m^2/g). At the carbonization, the superheated assistance provided a satisfactory porosity for the activation stage. On the other hand, the highest iodine uptake originates from the S–SS sample (870 mg/g). When a comparison was conducted between the SS–S and S–SS, narrower throat pores and deeply–excavated volumes caused surface area increments, with small to large porous size shifts having an effect on iodine adsorption. The enhanced active site for the adsorption of large organic types, such as iodine, by the decrease in pore volume as previously reported [58], was probably due to a shift in the distribution to the mesoporosity, as the present study suggests. The shift distribution to mesopores favoured adsorbate transfer and reduced diffusion blocking [43]. In fact, the results deviate as expected previously, and surface area depressed by superheating shifting to large mesopores for increased iodine adsorption. For the iodine adsorption application, micro pores and/or meso pores have a significant role [59].

3.5. Activated Carbon Structure

Based on Figures 5 and S4, almost all activated carbons had an aromatic structure reflection, denoted by varying amplitudes at 2–theta 24 and 44°, according to the planes of (002) and (100). Graphene planes (002) was at 2-theta 26° [60], subsequently indicating that the activated carbon was below it. The variation in reflection shape also originated from structural changes elicited by each activating agent. Saturation and superheating provided almost similar patterns, although superheated treatments still created supplementary peaks. This was probably correlated with the ash content increment after activation, corresponding to the burn–off effect [61]. The two broadened peaks of S–SS approximated to crystalline size perpendicular to the aromatic layer. When compared to reduced macroporosity (Table S1), this pathway led to high iodine adsorption capacity. When porosity and crystallinity were aligned, a narrow mesopores size and enhanced crystalline intensity provided an enlarged BET by saturation and superheated physical activation.

The XRD parameters are summarized in Table 2. The degree of crystallinity was shown by the XRD diffraction pattern, the amorphous structure of two peaks and the weak diffraction shifted according to the specified modification [62]. The amorphous structure was derived from lignin, which remained at a high temperature [63]. Three types of activators successfully transformed the 2-theta diffraction angle to reduce d and increase planarity. The narrowing of the curve which results in an increase in the degree of crystallinity is marked by narrow and sharp peaks [64]. The thermal activator (T), steam (S) and superheated (SS) gradually narrowed d (002) and d (100). For activator T alone, d (002) was shifted to 0.381, 0.373, and 0.370 nm. The same pattern applies to SS activators. The new finding of this study is in the activation of S derived from SS pyrochar precursor (SS–S samples). The 2–theta angle of 26.72°, d (002) 0.3333 nm and crystallinity of 23.56% resulted in the highest BET (642 m^2/g). The SS–S samples had the highest 2–theta and the narrowest spacing to produce steady porosity evolution.

3.6. Surface Topography

The SEM image is shown in Figure 6. Activated carbon prepared by saturation and superheating has better pore development than thermal alone. Pyrochar assisted by superheating showed a wide pore diameter. However, the creation of small–holes by steam activation adorns the product surface for an increase in the BET surface area, as in the SS–S sample. Saturated–assisted biochar showed a reduced pore diameter compared to superheated–assisted pyrochar. However, superheated activation results in the widening of the pores to provide an active site for iodine adsorption as indicated in the S–SS sample. Activated carbon S–SS had the highest iodine adsorption, as demonstrated in Figure 4. Pyrochar derived from thermal treatment showed a more irregular structure and showed a footprint of the release of non–C fraction, particularly shown by sample T–T. In general, steam-assisted activation (saturation and superheated) showed more satisfactory creation and pore development than thermal treatment alone.

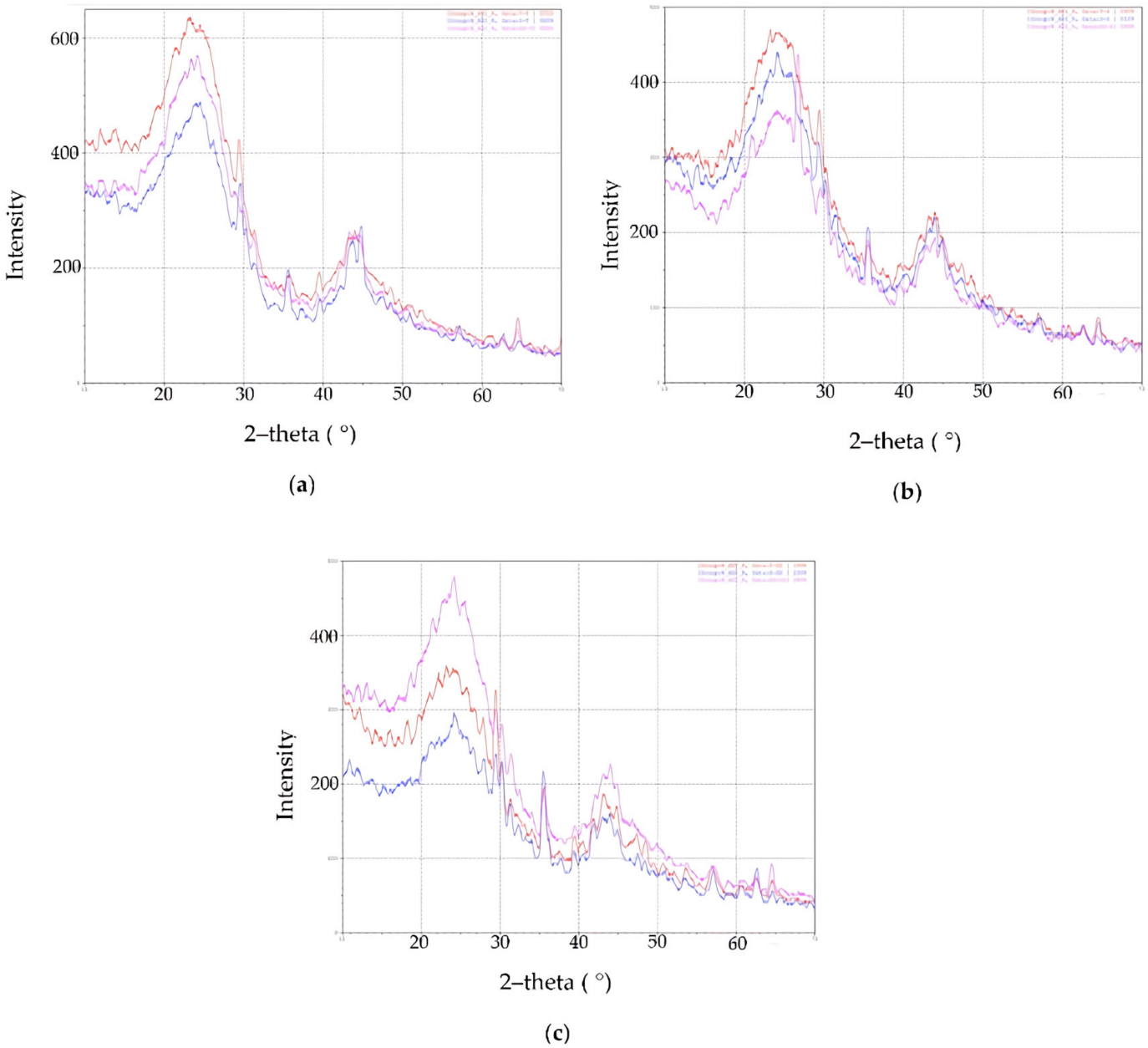


Figure 5. X-ray diffractogram of the prepared activated carbon: (**a**) thermal activation (red line T–T, blue line S–T, purple line SS–T); (**b**) steam activation (red line T–S, purple line S–S, blue line SS–S); (**c**) superheated activation (red line T–SS, blue line S–SS, purple line SS–SS).

Table 2. XRD parameters of activated carbon prepared by thermal, saturation and superheating.

Samples	2θ $Lc_{(002)}$	$d_{(002)}$ (nm)	2θ $La_{(100)}$	$d_{(100)}$ (nm)	Lc (nm)	N	La (nm)	X (%)
T–T	23.30	0.3814	44.00	0.2056	1.2414	3.26	2.8500	21.29
T–S	23.80	0.3735	44.72	0.2024	1.6086	4.31	3.4210	21.59
T–SS	23.98	0.3707	44.75	0.2023	1.9851	5.35	3.8764	23.82
S–T	23.98	0.3707	43.36	0.2085	1.5065	4.06	5.2317	22.26
S–S	24.16	0.3680	43.86	0.2062	1.5070	4.10	4.6992	24.71
S–SS	24.94	0.3567	43.92	0.2059	1.6706	4.68	5.0529	23.08
SS–T	24.26	0.3665	43.16	0.2094	1.2303	3.36	6.3730	24.66
SS–S	26.72	0.3333	44.79	0.2021	1.3191	3.96	5.5577	23.56
SS–SS	25.58	0.3479	43.96	0.2058	1.2928	3.72	7.5968	32.76

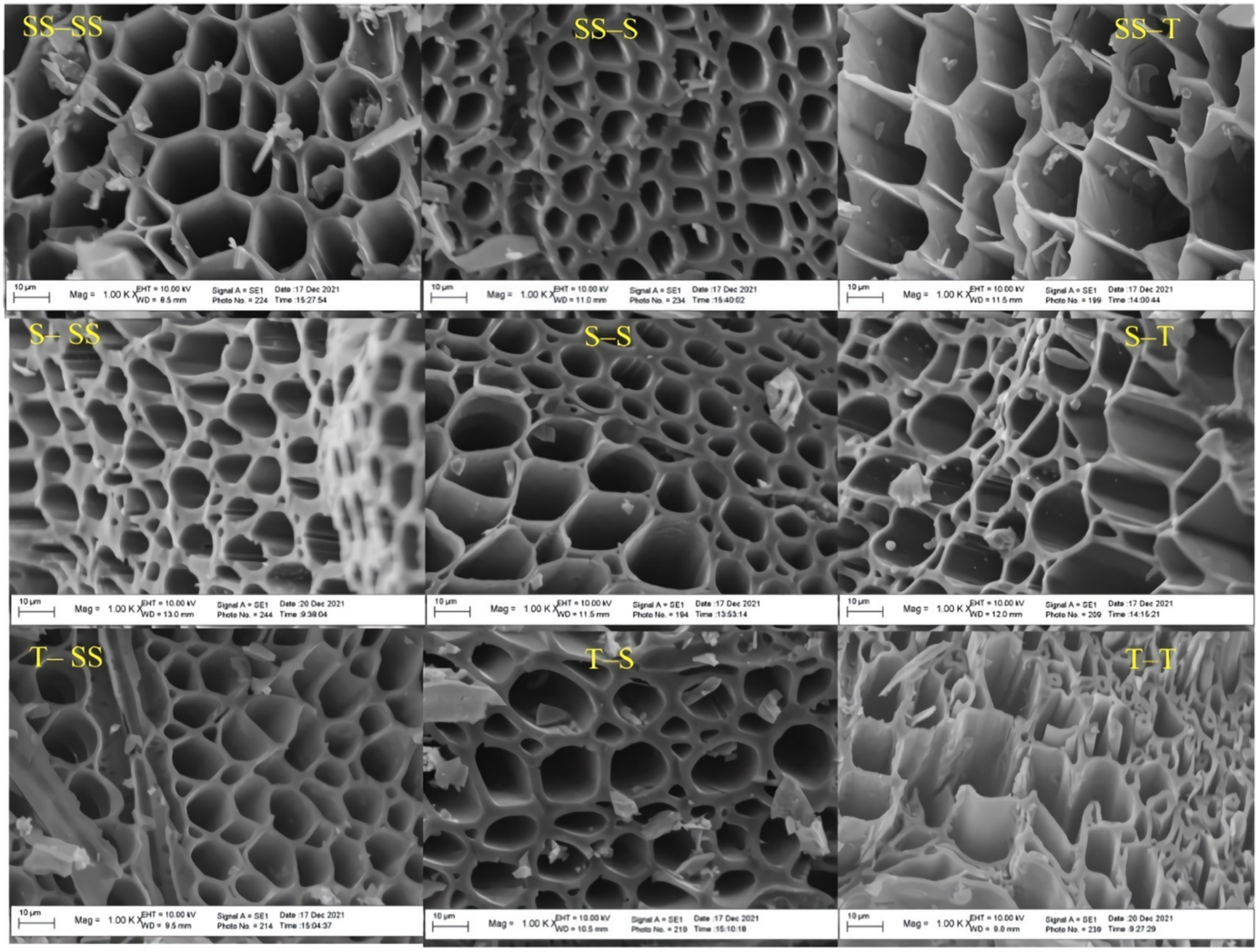


Figure 6. Scanning electron micrographs of prepared activated carbon.

3.7. Thermogravimetric (TGA)

The process parameters of the TGA analysis are summarized in Table 3. As a function of temperature, relative air mass and heat losses/rates were monitored by the DTG–DSC to define pyrolysis behaviours. The pyrolysis procedure in the present study was divided into four sections as follows: (1) initial heating until drying, (2) pre–drying to evaporate free water, (3) post and intermediate drying to remove bound water, volatiles and thermal transfer, and (4) thermal decomposition to release volatiles and light molecules while mass being degraded to 500 °C. In addition, a typical process was depicted by gases and pyrolysis oil resulting from thermally decomposed cellulose, hemicellulose, and lignin.

The pre–drying phase at 105 °C represented initial mass loss, where free water evaporation was carried out. The crude sample had the lowest mass loss (7.2%), while SS–S exhibiting that the highest experienced a massive decline. Superheating is an effective agent to remove the non-C fraction in the carbonization stage. In a typical endothermic reaction, dehydration and depolymerization decorate the reaction below a temperature of 300 °C [65].

Table 3. Summary of DTG-DSC.

Sample Code	Mass mg	% Mass Loss at ±105 °C	Tig		Tbo	Mass Loss at Tbo	Rmax			Onset Point		Offset Point		Point of Reaction		Tmax		Enthalpy (J/g)
			°C	%	°C	%	°C	mg/s	%	°C	min	°C	min	°C	min	°C	min	
Crude	7.92	7.2	285.1	12.9	562.3	87.6	323.2	0.0176	35.2	234.9	11.0	508.9	28.0	284.1	13.0	345.6	17.0	20,121
SS-SS	12.95	15.3	340.4	21.9	217.1	90.8	365.5	0.0213	33.8	320.8	19.0	472.4	30.0	345.9	20.0	368.5	22.0	28,013
S-SS	7.73	17.4	348.2	25.7	597.4	91.6	375.0	0.0197	45.4	328.6	19.0	434.8	27.0	354.8	21.0	382.0	23.0	37,004
T-SS	12.2	16.3	344.2	22.7	492.2	90.5	369.1	0.0236	36.7	325.0	19.0	456.1	29.0	345.7	20.0	374.5	22.0	23,614
SS-S	8.96	18.1	351.2	27.0	517.4	78.3	379.7	0.0160	46.9	333.0	20.0	479.4	30.0	358.4	21.0	384.3	23.0	30,485
S-S	25.28	15.0	321.7	17.1	510.9	75.1	348.8	0.0305	26.1	298.5	17.0	487.3	30.0	325.5	18.0	355.6	20.0	18,620
T-S	9.26	17.6	335.0	24.7	496.5	82.3	364.8	0.0175	40.5	315.6	18.0	471.1	29.0	344.5	20.0	370.4	22.0	34,224
SS-T	7.67	15.2	450.4	31.1	712.3	50.7	549.7	0.0114	74.1	511.9	32.0	652.3	42.0	548.4	34.0	568.9	36.0	48,543
S-T	15.61	10.5	434.5	18.3	568.1	44.8	571.6	0.0103	45.6	387.7	23.0	552.7	35.0	398.1	24.0	528.3	33.0	5,622
T-T	11.50	10.7	440.9	19.1	600.6	87.6	517.9	0.0192	61.7	406.9	25.0	568.6	36.0	459.3	28.0	531.2	33.0	31,384

Intermediate heating subsequently continued to 200 °C, which was an ignition temperature (Tig) for initial combustion. Raw samples had the fastest ignition at a low temperature of 285 °C, pursued by steam–activated samples (saturated and superheated) at 321–351 °C. Meanwhile, thermal has difficulty initiating sample combustion under a temperature of 430 °C. In the intermediate phase, some chemical constituents were released from the material. This study ascertains the degradation of the basic polymer up to a temperature of 500 °C, which is characterized by extreme weight loss. A typical decomposition of amorphous hemicellulose at low temperatures of 200–260 °C was accompanied by a long cellulose chain and benzene-propane from the lignin constituent at 240–350 and 280–500 °C, respectively [41].

In the fourth stage, active thermal decomposition occurred from Tig to final combustion temperature (Tbo) was assumed as extinguish point. The fastest and slowest decomposition phases originated from SS–SS and SS–T, respectively. The result clearly denotes some hypotheses: (1) samples were highly reactive to superheating in carbonization, and (2) thermal activation was inert against ash and volatile content, even at 800 °C. Thermal workings through the release of hydrocarbon bonds and interfering substances [66]. In addition, the first assumption was essentially in line with the previous study, through superheated treatment in the torrefaction process [35]. At 300–400 °C, almost all pyrolysis samples were oxidized as expressed by the onset point value. A summary and illustration of the DTG–DSC data are presented in Figure S2.

3.8. Functional Group of Activated Carbon

Since activated carbon adsorption properties are particularly unique, the surface function is essential to investigate. An FTIR analysis was based on the molar absorbance inversely proportional to the measured substance concentration, according to the Lambert–Beer law. Summary and detailed spectra of the FTIR analysis are shown in Table 4 and Figure S3.

Table 4. Functional groups and % transmittance of activated carbon.

Sample	O–H	C≡C	C=O	Alkanes	NO_2	C–N	C–O	Alkenes
T–SS	58.5	38.6	45.5	54.6	56.8	45.1	52.6	52.4
S–SS	70.1	46.5	54.3	62.3	65.4	53.1	59.9	59.2
SS–SS	58.5	38.6	45.5	54.6	56.4	45.1	57.7	52.3
T–S	63.2	40.0	45.8	53.2	57.8	46.2	52.7	52.3
S–S	137.5	65.9	77.5	68.4	90.8	68.4	68.4	81.3
SS–S	155.5	63.7	89.1	93.7	103.7	79.1	93.3	92.9
T–T	65.9	41.0	47.9	54.1	58.5	46.1	51.9	50.1
S–T	75.6	47.8	54.7	61.6	67.0	53.7	60.8	58.7
SS–T	97.2	59.0	66.8	74.2	80.1	64.7	72.0	68.0

O–H was a functional group of phenolic and alcohol compounds, and carboxylic acid with spectrum vibration intensity varied, subsequently indicating a high wide peak. The functional O–H indicated hydrogen bonds from carboxyl compounds, phenols, or alcohols. The transmittance increases or a decrease in absorbance indicated aromatic development [67]. The double bond (C=O) was identified in the wavenumber of 1.670–1.700 and a typical functional group encountered in activated carbon [68]. The 1.500–400 wavenumbers contained nitro (NO2), amides (CN), alcohols, ethers, esters (C–O), as well as the C–H alkanes and alkenes as shown in Fig.S.3. Activated carbon functional groups containing OH, C=O, and C–O played an important role in absorbing pollutants [69]. The surface functional groups containing oxygen also significantly influenced the chemical properties, such as hydrophobic surface properties [70].

4. Conclusions

A comparison of pyrolysis and activation agents was carried out in this study using a novel material, red calliandra. The results showed an increase in pyrochar porosity which was segmented by basic polymer decomposition, subsequently characterized by an increase in BET and iodine adsorption at 250, 350, and 500 °C, respectively. Small mesopores (2–10 nm) were produced by steam compared to large mesopores (10–50 nm) or macropores (>50 nm) by thermal assistance. Pore creation was severely disturbed by the ash content leading to blocking. Furthermore, superheated activation diverted the pore distribution to large mesopores for enhanced iodine adsorption compared to the saturation steam maintaining small mesopores for the increased BET surface area. Despite the expectations to increase the surface area, the superheated activation widened pores compared to saturation. The ultimate, structure, and morphology analysis confirmed the statements and were further explained by thermal pyrolytic behaviour in detail.

Supplementary Materials: The following supporting information can be downloaded at: https://www.mdpi.com/article/10.3390/en15186675/s1, Figure S1: Proximate property; Table S1: BJH pore distribution report; Figure S2: Thermogram analysis; Figure S3: The FTIR spectra; Figure S4: The XRD structure analysis: A Novel Mesoporous Activated Carbon Derived from *Calliandra calothyrsus* via Physical Activation: Saturation and Superheated.

Author Contributions: Conceptualization, N.A.S., D., D.S.N., A.M., G.P. and W.S.; Data curation, N.A.S. and L.E.; Formal analysis, N.A.S., S.D., L.E., D.H., S.W., A.S., D., G., S.K., D.A.I., Y., D.S.N., A.M. and G.P.; Funding acquisition, W.S.; Investigation, D.S.N., A.M. and G.P.; Project administration, N.A.S.; Validation, D.S.N., A.M., G.P. and W.S.; Writing—original draft, N.A.S., S.D., L.E., D.H., S.W., A.S., D., G., S.K., D.A.I., Y. and W.S.; Writing—review & editing, N.A.S. and W.S. All authors have read and agreed to the published version of the manuscript.

Funding: This work was funded by Directorate General of Higher Education, Research and Technology–Indonesian Ministry of Education, Culture, Research and Technolog, grant number 3824/IT3. L1/PT.01.03/P/B/2022.

Data Availability Statement: Data is contained within the article or Supplementary Material.

Acknowledgments: We would like to thank to IPB University, Indonesian National Research and Innovation Agency (BRIN), Center for Standardization of Sustainable Forest Management Instruments, Ministry of Environment and Forestry of the Republic of Indonesia for laboratory facilities. All author as main contributor in this manuscript.

Conflicts of Interest: The authors declare that they have no conflict of interest.

References

1. Jain, A.; Balasubramanian, R.; Srinivasan, M. Production of high surface area mesoporous activated carbons from waste biomass using hydrogen peroxide-mediated hydrothermal treatment for adsorption applications. *Chem. Eng. J.* **2015**, *273*, 622–629. [CrossRef]
2. Yuan, J.; Amano, Y.; Machida, M. Surface characterization of mesoporous biomass activated carbon modified by thermal chemical vapor deposition and adsorptive mechanism of nitrate ions in aqueous solution. *Colloids Surfaces A Physicochem. Eng. Asp.* **2021**, *616*, 126213. [CrossRef]

3. Ekanayake, U.M.; Rahmati, S.; Zhou, R.; Zhou, R.; Cullen, P.J.; O'Mullane, A.P.; MacLeod, J.; Ostrikov, K.K. Power-to-decarbonization: Mesoporous carbon-MgO nanohybrid derived from plasma-activated seawater salt-loaded biomass for efficient CO_2 capture. *J. CO2 Util.* **2021**, *53*, 101711. [CrossRef]
4. Khalil, K.M.; Elhamdy, W.A.; Mohammed, K.M.; Said, A.E.-A.A. Nanostructured P-doped activated carbon with improved mesoporous texture derived from biomass for enhanced adsorption of industrial cationic dye contaminants. *Mater. Chem. Phys.* **2022**, *282*, 125881.
5. Cheng, H.; Ye, G.; Wang, X.; Su, C.; Zhang, W.; Yao, F.; Wang, Y.; Jiao, Y.; Huang, H.; Ye, D. Micro-mesoporous carbon fabricated by Phanerochaete chrysosporium pretreatment coupling with chemical activation: Promoting effect and toluene adsorption performance. *J. Environ. Chem. Eng.* **2021**, *9*, 105054. [CrossRef]
6. Zhang, G.; Lei, B.; Chen, S.; Xie, H.; Zhou, G. Activated carbon adsorbents with micro-mesoporous structure derived from waste biomass by stepwise activation for toluene removal from air. *J. Environ. Chem. Eng.* **2021**, *9*, 105387. [CrossRef]
7. Khalil, K.M.; Elhamdy, W.A.; Elsamahy, A.A. Biomass derived P−doped activated carbon as nanostructured mesoporous adsorbent for chromium(VI) pollutants with pronounced functional efficiency and recyclability. *Colloids Surfaces A: Physicochem. Eng. Asp.* **2022**, *641*, 128553. [CrossRef]
8. Neolaka, Y.A.; Lawa, Y.; Naat, J.; Riwu, A.A.; Darmokoesoemo, H.; Widyaningrum, B.A.; Iqbal, M.; Kusuma, H.S. Indonesian Kesambi wood (*Schleichera oleosa*) activated with pyrolysis and H_2SO_4 combination methods to produce mesoporous activated carbon for Pb(II) adsorption from aqueous solution. *Environ. Technol. Innov.* **2021**, *24*, 101997.
9. Liou, T.-H. Development of mesoporous structure and high adsorption capacity of biomass-based activated carbon by phosphoric acid and zinc chloride activation. *Chem. Eng. J.* **2010**, *158*, 129–142. [CrossRef]
10. Saputra, N.A.; Saputra, I.S.; Yuniarti, K. Andianto Preparation and characterization of Gigantochloa robusta activated carbon to reduce COD levels of pharmaceutical waste. *IOP Conf. Ser. Mater. Sci. Eng.* **2020**, *935*. [CrossRef]
11. Rutherford, D.W.; Wershaw, R.L.; Rostad, C.E.; Kelly, C.N. Effect of formation conditions on biochars: Compositional and structural properties of cellulose, lignin, and pine biochars. *Biomass Bioenergy* **2012**, *46*, 693–701. [CrossRef]
12. Lewoyehu, M. Comprehensive review on synthesis and application of activated carbon from agricultural residues for the remediation of venomous pollutants in wastewater. *J. Anal. Appl. Pyrolysis* **2021**, *159*, 105279.
13. Joshi, S.; Shrestha, R.G.; Pradhananga, R.R.; Ariga, K.; Shrestha, K.L. High surface area nanoporous activated carbons materials. *J. Carbon Res.* **2022**, *8*, 2. [CrossRef]
14. Fan, Y.; Yang, X.; Zhu, B.; Liu, P.-F.; Lu, H.-T. Micro-mesoporous carbon spheres derived from carrageenan as electrode material for supercapacitors. *J. Power Sources* **2014**, *268*, 584–590. [CrossRef]
15. Rustamaji, H.; Prakoso, T.; Devianto, H.; Widiatmoko, P.; Saputera, W.H. Urea nitrogenated mesoporous activated carbon derived from oil palm empty fruit bunch for high-performance supercapacitor. *J. Energy Storage* **2022**, *52*, 104724.
16. Ma, X.; Yang, H.; Yu, L.; Chen, Y.; Li, Y. Preparation, Surface and Pore Structure of High Surface Area Activated Carbon Fibers from Bamboo by Steam Activation. *Materials* **2014**, *7*, 4431–4441. [CrossRef]
17. Pallarés, J.; González-Cencerrado, A.; Arauzo, I. Production and characterization of activated carbon from barley straw by physical activation with carbon dioxide and steam. *Biomass Bioenergy* **2018**, *115*, 64–73. [CrossRef]
18. Chen, D.; Chen, X.; Sun, J.; Zheng, Z.; Fu, K. Pyrolysis polygeneration of pine nut shell: Quality of pyrolysis products and study on the preparation of activated carbon from biochar. *Bioresour. Technol.* **2016**, *216*, 629–636. [CrossRef]
19. Bardestani, R.; Kaliaguine, S. Steam activation and mild air oxidation of vacuum pyrolysis biochar. *Biomass-Bioenergy* **2017**, *108*, 101–112. [CrossRef]
20. Alvarez, J.; Lopez, G.; Amutio, M.; Bilbao, J.; Olazar, M. Upgrading the rice husk char obtained by flash pyrolysis for the production of amorphous silica and high quality activated carbon. *Bioresour. Technol.* **2014**, *170*, 132–137. [CrossRef]
21. Yi, H.; Nakabayashi, K.; Yoon, S.-H.; Miyawaki, J. Pressurized physical activation: A simple production method for activated carbon with a highly developed pore structure. *Carbon* **2021**, *183*, 735–742. [CrossRef]
22. Zaini, M.A.A.; Zhi, L.L.; Hui, T.S.; Amano, Y.; Machida, M. Effects of physical activation on pore textures and heavy metals removal of fiber-based activated carbons. *Mater. Today Proc.* **2020**, *39*, 917–921. [CrossRef]
23. Williams, P.; Reed, A. Development of activated carbon pore structure via physical and chemical activation of biomass fibre waste. *Biomass-Bioenergy* **2006**, *30*, 144–152. [CrossRef]
24. Powell, M.H.; Roshetko, J.M. International workshop on the Genus Calliandra. In *International Workshop on the Genus Calliandra*; Winrock International: Bogor, Indonesia, 1996.
25. Chamberlain, J.R. *Calliandra Calothyrsus: An Agroforestry Tree for the Humid Tropics 40*; Oxford Forestry Institute, University of Oxford: Oxford, UK, 2001.
26. Adaganti, S.Y.; Kulkarni, B.M.; Desai, G.P.; Shanmukhappa, S. Effect of hydrothermal explosion pretreatment on the composition and structure of Calliandra calothyrsus shrub—A lignocellulosic biomass. *Int. J. Renew. Sustain. Energy* **2014**, *3*, 1–5. [CrossRef]
27. Hendrati, R.L.; Hidayati, N. Budidaya kaliandra (*Calliandra calothyrsus*) Untuk Bahan Baku Sumber Energi. Cetakan 1. IPB Press: Bogor, Indonesia, 2014.
28. Haqiqi, M.T.; Yuliansyah; Suwinarti, W.; Amirta, R. Response surface methodology to simplify calculation of wood energy potency from tropical short rotation coppice species. *IOP Conf. Ser. Earth Environ. Sci.* **2018**, *144*, 012041. [CrossRef]

29. Cagnon, B.; Py, X.; Guillot, A.; Stoeckli, F.; Chambat, G. Contributions of hemicellulose, cellulose and lignin to the mass and the porous properties of chars and steam activated carbons from various lignocellulosic precursors. *Bioresour. Technol.* **2009**, *100*, 292–298. [CrossRef]
30. Rouatbi, M.; Duquenoy, A.; Giampaoli, P. Extraction of the essential oil of thyme and black pepper by superheated steam. *J. Food Eng.* **2007**, *78*, 708–714. [CrossRef]
31. Sagehashi, M.; Miyasaka, N.; Shishido, H.; Sakoda, A. Superheated steam pyrolysis of biomass elemental components and Sugi (*Japanese cedar*) for fuels and chemicals. *Bioresour. Technol.* **2006**, *97*, 1272–1283. [CrossRef]
32. Berghel, J.; Renström, R. Superheated steam drying of sawdust in continuous feed spouted beds—A design perspective. *Biomass-Bioenergy* **2014**, *71*, 228–234. [CrossRef]
33. Xu, K.; Tu, D.; Chen, T.; Zhong, T.; Lu, J. Effects of environmental-friendly modified rubber seed shell on the comprehensive properties of high density polyethylene/rubber seed shell composites. *Ind. Crop. Prod.* **2016**, *91*, 132–141. [CrossRef]
34. Behera, G.; Sutar, P. A comprehensive review of mathematical modeling of paddy parboiling and drying: Effects of modern techniques on process kinetics and rice quality. *Trends Food Sci. Technol.* **2018**, *75*, 206–230. [CrossRef]
35. Zhang, D.; Chen, X.; Qi, Z.; Wang, H.; Yang, R.; Lin, W.; Li, J.; Zhou, W.; Ronsse, F. Superheated steam as carrier gas and the sole heat source to enhance biomass torrefaction. *Bioresour. Technol.* **2021**, *331*, 124955. [CrossRef] [PubMed]
36. Zhang, D.; Han, P.; Yang, R.; Wang, H.; Lin, W.; Zhou, W.; Yan, Z.; Qi, Z. Fuel properties and combustion behaviors of fast torrefied pinewood in a heavily loaded fixed-bed reactor by superheated steam. *Bioresour. Technol.* **2021**, *342*, 125929. [CrossRef] [PubMed]
37. Dence, C.W. The Determination of Lignin. In *Methods in Lignin Chemistry*; Lin, S.Y., Dence, C.W., Eds.; Springer: Berlin/Heidelberg, Germany, 1992; pp. 33–61.
38. Yoshihara, K.; Kobayashi, T.; Fujii, T.; Akamatsu, I. A novel modification of Klason lignin quantitaitve method. *Jpn. Tappi J.* **1984**, *38*, 466–475. [CrossRef]
39. Niksiar, A.; Nasernejad, B. Activated carbon preparation from pistachio shell pyrolysis and gasification in a spouted bed reactor. *Biomass-Bioenergy* **2017**, *106*, 43–50. [CrossRef]
40. Zhang, Y.-J.; Xing, Z.-J.; Duan, Z.-K.; Li, M.; Wang, Y. Effects of steam activation on the pore structure and surface chemistry of activated carbon derived from bamboo waste. *Appl. Surf. Sci.* **2014**, *315*, 279–286. [CrossRef]
41. Danish, M.; Ahmad, T. A review on utilization of wood biomass as a sustainable precursor for activated carbon production and application. *Renew. Sustain. Energy Rev.* **2018**, *87*, 1–21.
42. Al-Wabel, M.I.; Al-Omran, A.; El-Naggar, A.H.; Nadeem, M.; Usman, A.R. Pyrolysis temperature induced changes in characteristics and chemical composition of biochar produced from conocarpus wastes. *Bioresour. Technol.* **2013**, *131*, 374–379. [CrossRef]
43. Su, Y.; Liu, L.; Zhang, S.; Xu, D.; Du, H.; Cheng, Y.; Wang, Z.; Xiong, Y. A green route for pyrolysis poly-generation of typical high ash biomass, rice husk: Effects on simultaneous production of carbonic oxide-rich syngas, phenol-abundant bio-oil, high-adsorption porous carbon and amorphous silicon dioxide. *Bioresour. Technol.* **2019**, *295*, 122243. [CrossRef]
44. Angın, D. Effect of pyrolysis temperature and heating rate on biochar obtained from pyrolysis of safflower seed press cake. *Bioresour. Technol.* **2013**, *128*, 593–597. [CrossRef]
45. Enders, A.; Hanley, K.; Whitman, T.; Joseph, S.; Lehmann, J. Characterization of biochars to evaluate recalcitrance and agronomic performance. *Bioresour. Technol.* **2012**, *114*, 644–653. [CrossRef] [PubMed]
46. Luo, L.; Xu, C.; Chen, Z.; Zhang, S. Properties of biomass-derived biochars: Combined effects of operating conditions and biomass types. *Bioresour. Technol.* **2015**, *192*, 83–89. [CrossRef]
47. Ghani, W.A.W.A.K.; Mohd, A.; da Silva, G.; Bachmann, R.T.; Taufiq-Yap, Y.H.; Rashid, U.; Al-Muhtaseb, A.H. Biochar production from waste rubber-wood-sawdust and its potential use in C sequestration: Chemical and physical characterization. *Ind. Crop. Prod.* **2013**, *44*, 18–24. [CrossRef]
48. Yakaboylu, O.; Albrecht, I.; Harinck, J.; Smit, K.; Tsalidis, G.-A.; Di Marcello, M.; Anastasakis, K.; de Jong, W. Supercritical water gasification of biomass in fluidized bed: First results and experiences obtained from TU Delft/Gensos semi-pilot scale setup. *Biomass-Bioenergy* **2018**, *111*, 330–342. [CrossRef]
49. Sumathi, S.; Bhatia, S.; Lee, K.T.; Mohamed, A.R. Optimization of microporous palm shell activated carbon production for flue gas desulphurization: Experimental and statistical studies. *Bioresour. Technol.* **2009**, *100*, 1614–1621. [CrossRef] [PubMed]
50. Manyà, J.J.; Azuara, M.; Manso, J.A. Biochar production through slow pyrolysis of different biomass materials: Seeking the best operating conditions. *Biomass-Bioenergy* **2018**, *117*, 115–123. [CrossRef]
51. Chen, F.-X.; Gong, P.; Zhang, H.-K.; Bai, X.-H.; Gao, Y.-F.; Zhou, A.-N. Biomass Pyrolysis of Helianthus annuus Stems: Qualitative and Quantitative Study Based on Py-GC/MS. *BioResources* **2016**, *11*, 8589–8614. [CrossRef]
52. Chen, Y.; Yang, H.; Wang, X.; Zhang, S.; Chen, H. Biomass-based pyrolytic polygeneration system on cotton stalk pyrolysis: Influence of temperature. *Bioresour. Technol.* **2011**, *107*, 411–418. [CrossRef]
53. Li, W.; Yang, K.; Peng, J.; Zhang, L.; Guo, S.; Xia, H. Effects of carbonization temperatures on characteristics of porosity in coconut shell chars and activated carbons derived from carbonized coconut shell chars. *Ind. Crop. Prod.* **2008**, *28*, 190–198. [CrossRef]
54. Zhu, X.; Li, C.; Li, J.; Xie, B.; Lü, J.; Li, Y. Thermal treatment of biochar in the air/nitrogen atmosphere for developed mesoporosity and enhanced adsorption to tetracycline. *Bioresour. Technol.* **2018**, *263*, 475–482.
55. Sahin, Ö.; Saka, C. Preparation and characterization of activated carbon from acorn shell by physical activation with H_2O–CO_2 in two-step pretreatment. *Bioresour. Technol.* **2013**, *136*, 163–168. [CrossRef]

56. Maneerung, T.; Liew, J.; Dai, Y.; Kawi, S.; Chong, C.; Wang, C.H. Activated carbon derived from carbon residue from biomass gasification and its application for dye adsorption: Kinetics, isotherms and thermodynamic studies. *Bioresour. Technol.* **2016**, *200*, 350–359. [CrossRef] [PubMed]
57. Dong, L.; Liu, W.; Jiang, R.; Wang, Z. Physicochemical and porosity characteristics of thermally regenerated activated carbon polluted with biological activated carbon process. *Bioresour. Technol.* **2014**, *171*, 260–264. [CrossRef]
58. An, D.; Guo, Y.; Zou, B.; Zhu, Y.; Wang, Z. A study on the consecutive preparation of silica powders and active carbon from rice husk ash. *Biomass-Bioenergy* **2011**, *35*, 1227–1234. [CrossRef]
59. Xu, Z.; Zhang, Q.; Lin, P.; Gao, Y.; Wen, Y.; Li, K.; Li, L. Oxygen-rich microporous carbons with exceptionally high adsorption of iodine. *Mater. Chem. Phys.* **2022**, *285*, 126193. [CrossRef]
60. Kanjana, K.; Harding, P.; Kwamman, T.; Kingkam, W.; Chutimasakul, T. Biomass-derived activated carbons with extremely narrow pore size distribution via eco-friendly synthesis for supercapacitor application. *Biomass-Bioenergy* **2021**, *153*, 106206. [CrossRef]
61. Subramanian, S.; Pande, G.; De Weireld, G.; Giraudon, J.-M.; Lamonier, J.-F.; Batra, V.S. Sugarcane bagasse fly ash as an attractive agro-industry source for VOC removal on porous carbon. *Ind. Crop. Prod.* **2013**, *49*, 108–116. [CrossRef]
62. Liu, X.; Zhang, S.; Luo, H.; Zhang, Y.; Xu, Q.; Zhang, Z.; Xu, H.; Wang, Z. Biomass activated carbon supported with high crystallinity and dispersion Fe 3 O 4 nanoparticle for preconcentration and effective degradation of methylene blue. *J. Taiwan Inst. Chem. Eng.* **2017**, *81*, 265–274. [CrossRef]
63. Pari, G.; Sofyan, K.; Syafii, W.; Buchari, B.; Yamamoto, H. Kajian Struktur Arang Dari Lignin. *J. Penelit. Has. Hutan* **2006**, *24*, 9–20. [CrossRef]
64. Shvalagin, V.; Kuchmiy, S.; Skoryk, M.; Bondarenko, M.; Khyzhun, O. Acid treated crystalline graphitic carbon nitride with improved efficiency in photocatalytic ethanol oxidation under visible light. *Mater. Sci. Eng. B* **2021**, *271*, 115304. [CrossRef]
65. Parthasarathy, P.; Narayanan, K.S.; Arockiam, L. Study on kinetic parameters of different biomass samples using thermo-gravimetric analysis. *Biomass-Bioenergy* **2013**, *58*, 58–66. [CrossRef]
66. Mohammad-Khah, A.; Ansari, R. Activated charcoal: Preparation, characterization and applications: A review article. *Int. J. Chem. Tech. Res.* **2009**, *1*, 859–864.
67. Allwar, A.; Winarsi, R.; Fitriyani, N.; Merdekawati, K. Characterization and Application of Activated Carbon from Oil Palm Shell Prepared By Physical Activation and Nitric Acid for the Removal of Phenol and 2-Chlorophenol. *Int. J. Sci. Res.* **2017**, 1528–1534.
68. Maulina, S.; Mentari, V.A. Comparison of Functional Group and Morphological Surface of Activated Carbon from Oil Palm Fronds Using Phosphoric Acid (H_3PO_4) and Nitric Acid (HNO_3) as an Activator. *IOP Conf. Ser. Mater. Sci. Eng.* **2019**, *505*, 012023. [CrossRef]
69. Shu, J.; Cheng, S.; Xia, H.; Zhang, L.; Peng, J.; Li, C.; Zhang, S. Copper loaded on activated carbon as an efficient adsorbent for removal of methylene blue. *RSC Adv.* **2017**, *7*, 14395–14405. [CrossRef]
70. García, J.R.; Sedran, U.; Zaini, M.A.A.; Zakaria, Z.A. Preparation, characterization, and dye removal study of activated carbon prepared from palm kernel shell. *Environ. Sci. Pollut. Res.* **2017**, *25*, 5076–5085. [CrossRef] [PubMed]